

Mapping the Feasible Design Space of the Nanoparticle Field Extraction Thruster

IEPC-2009-004

*Presented at the 31st International Electric Propulsion Conference,
University of Michigan • Ann Arbor, Michigan • USA
September 20 – 24, 2009*

Thomas M. Liu^{*}, Gregory L. Wagner[†], Alec D. Gallimore[‡], and Brian E. Gilchrist[§]
University of Michigan, Ann Arbor, MI, 48109, USA

and

Peter Y. Peterson^{**}
ElectroDynamic Applications, Inc., Ann Arbor, MI, 48105, USA

Contact charging of micro- and nano-particles affords the Nanoparticle Field Extraction Thruster (NanoFET) flexibility to adjust its propellant's specific charge without an inherent impact on efficiency. Other than the particle size, two features in NanoFET's design also govern the range of achievable specific charges: the gate electrode configuration, which sets the charging electric fields and the resulting particle charge, and the particle mass density. Electrostatic simulations for various gate electrode configurations were conducted in COMSOL Multiphysics® to provide general scaling relations for the acquired particle charge as a function of gate geometry as well as particle size and proximity. The simulation results suggest that configurations with smaller gate aspect ratios, smaller relative particle sizes (compared to gate length scales), and larger extractor spacing-to-diameter ratios provide greater charging. The use of low mass density or hollow particles also enhances NanoFET's specific charge and gives the potential for moderate specific impulse and high thrust-to-power performance. Precise thrust control may also be possible using NanoFET's piezoelectric feed system to facilitate particle passage through the charging sieves, enable particle extraction, and regulate the mass flow rate.

Nomenclature

a_0	=	distance of closest approach
B	=	integrated field enhancement factor
d	=	particle diameter
D_G	=	gate orifice diameter
D_G/H	=	gate aspect ratio
E_L	=	particle liftoff electric field
E_s	=	electric field at particle surface
E_0	=	background electric field
f	=	frequency
F_E	=	electrostatic force

* Graduate Student, Aerospace Engineering, liutm@umich.edu

† Graduate Student, Aerospace Engineering, greglw@umich.edu

‡ Arthur F. Thurnau Professor, Aerospace Engineering & Applied Physics, alec.gallimore@umich.edu

§ Professor, Electrical Engineering & Space Systems, gilchrst@umich.edu

** Director of Research, peterson@edapplications.com

F_R	= net force restraining particles from extraction
g_0	= sea-level gravitational acceleration
H	= inter-electrode gap
H_A	= Hamaker constant
I_{sp}	= specific impulse
$(I_{sp})_h$	= specific impulse of hollow particle
$(I_{sp})_s$	= specific impulse of solid particle
m	= particle mass
m_h	= hollow particle mass
m_s	= solid particle mass
q	= particle charge
q_0	= saturation particle charge from Félici's model
q_1	= saturation particle charge in parallel-electrode configuration
q_2	= saturation particle charge in gated-electrode configuration
q_{2p}	= saturation particle charge in gated-electrode configuration with proximal particles
q/m	= particle specific charge
$(q/m)_h$	= hollow particle specific charge
$(q/m)_s$	= solid particle specific charge
R	= inter-particle distance
r	= radial position
t	= gate electrode thickness
t_w	= shell wall thickness
T_0	= single extractor thrust
T/P	= thrust-to-power
V	= applied voltage
V_a	= acceleration potential
x_{ppk}	= piezoelectric peak-to-peak oscillation amplitude
z	= axial position
D	= electric displacement field
E	= electric field
n	= surface normal unit vector
α_{isp}	= specific impulse enhancement factor
$\alpha_{q/m}$	= specific charge enhancement factor
α_{10}	= charging factor for parallel-electrode configuration
α_{20}	= net charging factor for gated-electrode configuration
α_{21}	= charging factor for gated-electrode configuration
α_{2p}	= charging factor for gated-electrode configuration with proximal particles
α_{2p0}	= net charging factor for gated-electrode configuration with proximal particles
β	= field enhancement factor
γ	= image charge factor
ε	= permittivity
η	= thruster efficiency
θ	= polar angle
ρ	= charge density
ρ_h	= hollow particle mass density
ρ_s	= solid particle mass density
ϕ	= electric potential

I. What Is NanoFET?

TRENDS in micro- and nano- in-space propulsion systems are making the logical progression towards devices with high efficiency, wide throttleability, small footprints, and low mass to enable deployment of ever smaller and more versatile fleets of spacecraft. The Nanoparticle Field Extraction Thruster (NanoFET) is one such propulsion technology being developed for pico- to small satellite applications.

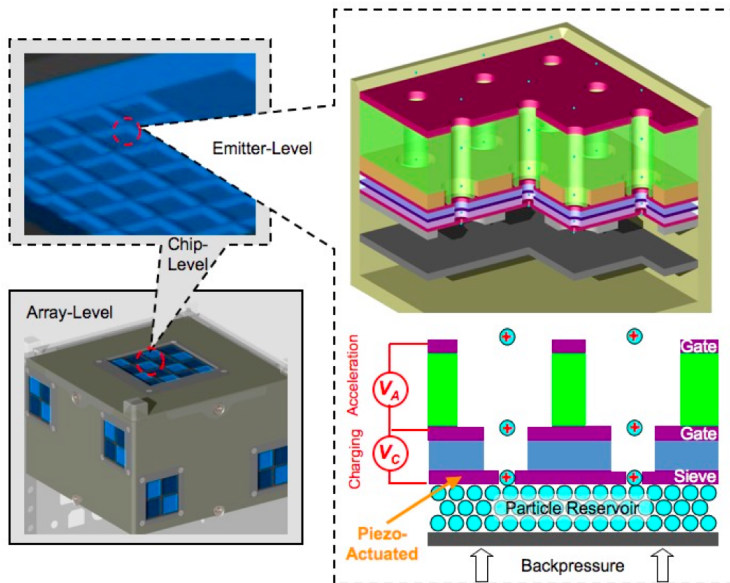


Figure 1. Concept views of NanoFET. Scalability is shown from the emitter (upper right: particles in reservoir not shown; lower right: cross-sectional view) up to the chip (upper left) and array (lower left) size scales. An integrated NanoFET propulsion module, including main and attitude control thrusters along with the propellant, is shown (lower left) taking up half the volume of a 1-unit cubesat.

While similar in operation to colloid thrusters, NanoFET does not rely on droplet formation and extraction as the source of propellant. Instead, the NanoFET system electrostatically charges and accelerates pre-fabricated, solid micro- and nano-particles. As shown conceptually in Figure 1, backpressure feeds the particle propellant in dry powder form towards the charging sieve. There, particle aggregates are dispersed upon passage through the sieve with the aid of piezoelectric-induced inertial forces. Individual particles undergo contact charging and are subsequently accelerated by the electric fields generated by stacked electrode gates. Potential bipolar operations would eliminate the need for a separate neutralizer since NanoFET would be self-neutralizing. By using micro/nano-electromechanical systems (MEMS/NEMS) fabrication processes, NanoFET achieves a compact, flat-panel configuration that is potentially scalable for a variety of mission needs.¹

With the propellant electrostatically charged rather than ionized, NanoFET can tune the propellant's charge state via the charging electric field. Unlike multiple ionization processes that suffer from

increasing ionization costs, NanoFET can adjust its propellant's specific charge q/m without an inherent impact on efficiency. Because specific impulse $I_{sp} \propto (q/m)^{1/2}$ as well as the acceleration potential, NanoFET may be considered a variable- I_{sp} thruster whose performance may be optimized at each point during an orbit maneuver to minimize propellant use or trip time or to accomplish dynamic retasking of the host spacecraft.²

An alternative configuration for NanoFET exists in which suspended particles, transported in a recirculating microfluidic feed system, are electrostatically charged and extracted from a low vapor pressure liquid reservoir via stacked electrode gates.³ By using dry particles, the liquid reservoir may be eliminated, thus improving thruster specific mass. Liquid-associated concerns are also bypassed, including maintaining a stable liquid-vacuum interface during thruster operations, minimizing particle wetting and the resultant fluid loss during particle extraction, accommodating space charge limits due to viscous drag in the liquid, and maintaining liquid purity from gas and particulate contamination that may lead to electrical arcing and shorts. The remainder of this paper is devoted to NanoFET's dry particle configuration.

The following sections examine two key challenges NanoFET faces in using dry particulate propellant:

- 1) How can specific charge be controlled to meet propulsive performance targets with reasonable acceleration potentials?
- 2) How can particle-particle cohesive forces and particle-electrode adhesive forces be overcome to permit charged particle extraction?

II. Controlling Propellant Specific Charge

The propellant specific charge (i.e., charge-to-mass ratio) may be controlled by adjusting either the particle charge or mass. Since $I_{sp} = g_0^{-1}(2V_a q/m)^{1/2}$, larger specific charges permit lower acceleration potentials V_a to be used to meet a given I_{sp} target; this reduction in operating voltages could simplify power system designs and improve operational reliability.

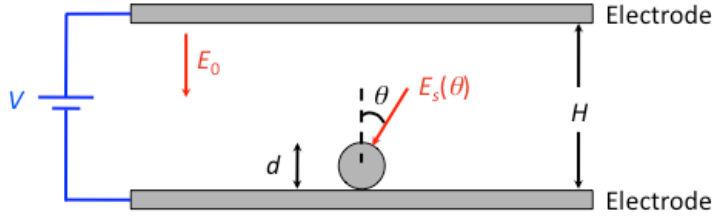


Figure 2. Particle charging in parallel-electrode configuration. *Electrode edge effects on the particle are assumed to be negligible.*

A. Particle Charging in NanoFET

Félici's analytical model for the saturation charge q_0 acquired by an isolated, spherical particle of diameter d in contact with a charging electrode and exposed to a uniform electric field E_0 (in the absence of particle focusing and edge effects) is

$$q_0 = \frac{\pi^3}{6} \epsilon E_0 d^2, \quad (1)$$

where ϵ is the permittivity of the medium about the particle.⁴ The charging field at the particle surface must be below the ion field evaporation ($\sim 10^4$ V/ μm) or electron field emission ($\sim 10^3$ V/ μm) thresholds for positively and negatively charged particles, respectively. For a spherical particle with uniform surface charge density, the particle charge q is

$$q = \pi \epsilon E_s d^2, \quad (2)$$

where E_s is the surface electric field. Comparing Equations 1 and 2 suggest that E_0 should be no more than 60% of the field emission/evaporation limit.⁵

Félici's model has been experimentally validated via dynamic and current measurements of particles (albeit at larger sizes than proposed for NanoFET) charged in a parallel-electrode configuration (Figure 2).^{6,7} In these studies, a particle lifts off the bottom electrode and moves towards the upper electrode if the electrostatic force acting on the charged particle is greater than the restraining forces. Upon contact with the upper electrode, the particle is charged opposite its initial polarity and is directed back towards the bottom electrode. The sequence then repeats, resulting in particle oscillations between the plates. Félici's model is valid for the parallel-electrode configuration provided that 1) the time scale associated with particle charge transfer to the surrounding medium is large compared to the oscillation period, 2) the particles achieve saturation charging prior to liftoff, and 3) the particles are small compared to the inter-electrode gap ($d \ll H$).

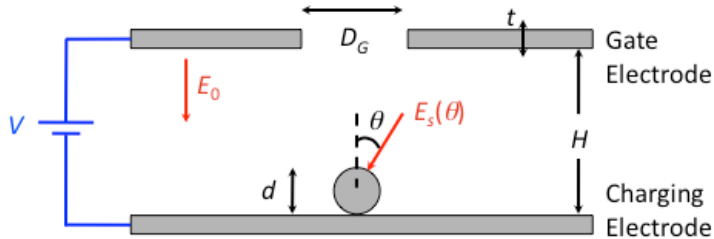


Figure 3. Particle charging in gated-electrode configuration. *Particle extraction is possible for $d/D_G < 1$. The gate orifice is assumed to be centered about the particle.*

The first two conditions are readily met using particles with high surface conductivities in a vacuum environment. As d/H increases, the particle field enhancement factor

$$\beta(\theta) \equiv \frac{E_s(\theta)}{E_0} \quad (3)$$

also increases, where $E_0 \equiv V/H$. For a constant E_0 , the resulting particle charge q_1 is greater than what is expected from Félici's model by the charging factor

$$\alpha_{10}(d, H) \equiv \frac{q_1}{q_0}, \quad (4)$$

which is within 5% of unity (i.e., exact agreement with Félici's model) for $d/H \leq 0.5$.⁸

In NanoFET, the upper electrode in Figure 2 is replaced with a gate electrode that permits particles to leave the system. This gated-electrode configuration is shown in Figure 3, with the gate orifice diameter D_G being greater than the particle diameter d to permit particle extraction.

1. Gated-Electrode Simulations

Electrostatic simulations were conducted in COMSOL Multiphysics®, a commercial finite element analysis software package, to investigate the impact of the gated-electrode configuration on particle charging. COMSOL’s electrostatic application mode, which solves Poisson’s equation ($\nabla^2\phi = -\rho/\epsilon$), has been previously used in numerical studies of particle contact charging with good agreement with analytical models.^{9,10} For these simulations, the geometries considered were not intended to be high-fidelity representations of NanoFET. Instead, simplified models were used to provide insights into scaling relations to aid optimization of NanoFET’s gate designs. As such, whereas NanoFET may have multiple gate electrodes, only the first gate is modeled as it has the dominant influence on the particle charging electric fields; subsequent gates chiefly supply inter-gate electric fields to accelerate particle propellant after it has already been charged and extracted. Further, NanoFET’s charging sieve is not modeled;

instead, as with the parallel-electrode configuration, particles are assumed to be in contact with a continuous charging electrode. Future work is intended to refine the simulations and explore sieve configuration effects on particle charging.

As shown in Figure 4, the simulation domain is axi-symmetric (r - z space) assuming the gate orifice is centered about the particle; $r = 0$ is defined as the axis of symmetry (centerline). A gate electrode of thickness $t = 0.1$ mm is modeled as an equipotential region of bias V placed 1 mm above a grounded charging electrode. These dimensions are not critical, since the simulation results are non-dimensionalized. Zero-charge/symmetry ($\mathbf{n} \cdot \mathbf{D} = 0$) boundary conditions are in place at the top and right ($z = 20$ mm and $r = 20$ mm, respectively) boundaries of the simulation domain; they are placed far enough away from the particles to avoid artificial boundary effects. The medium surrounding the particle (shaded region in Figure 4) has free-space permittivity, and the rigid, isolated, and grounded particle contacts the bottom electrode at the r - z space’s origin. A ring of particles of diameter d can be placed a distance R (center-to-center) around the central particle to examine proximal particle effects on charging.

As shown in Figure 4, an unstructured mesh of triangular elements is used for the simulation domain. Using COMSOL, the electric field at the particle surface can be mapped. Applying Gauss’s law ($q = \iint \epsilon \mathbf{E} \cdot d\mathbf{A}$) for the particle and utilizing azimuthal symmetry, the saturation charge q on the particle is

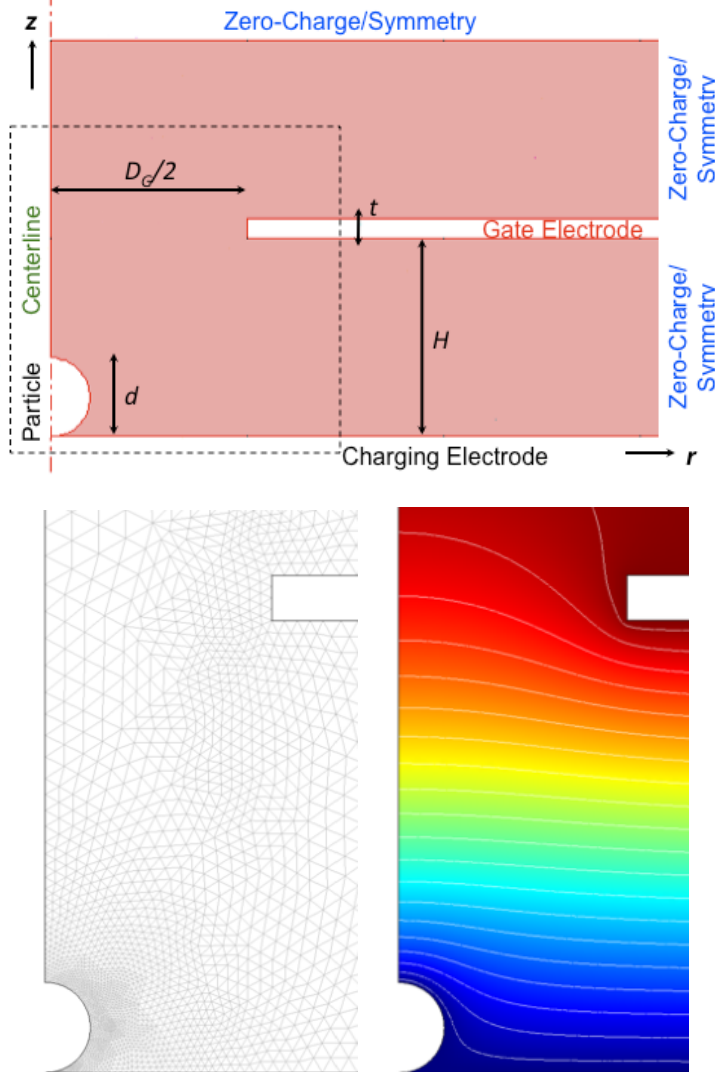


Figure 4. Representative COMSOL simulation for gated-electrode configuration. (Top) Boundary conditions shown in r - z simulation domain (not to scale). Representative unstructured mesh (bottom left) and solved electric potentials (bottom right) from simulation runs.

$$q = \frac{\pi}{2} \epsilon E_0 d^2 B, \quad (5)$$

where the integrated field enhancement factor B is defined as

$$B \equiv \int_0^\pi \beta(\theta) \sin \theta \, d\theta. \quad (6)$$

This formulation implicitly assumes that the particle charges classically and that quantum effects are not significant. Note that Félici's model corresponds to $B = \pi^2/3$.

2. Isolated Particle Charging

A constant background electric field $E_0 = V/H = 10 \text{ V}/\mu\text{m}$ was used to generate the results below. Since the inter-electrode spacing is fixed ($H = 1 \text{ mm}$) in the simulation domain, this simulation case also represents the application of a constant bias voltage ($V = 10 \text{ kV}$) in the simulation. Figure 5 shows representative electric field mapping results for isolated particles ($R/d \rightarrow \infty$) of various d/H .

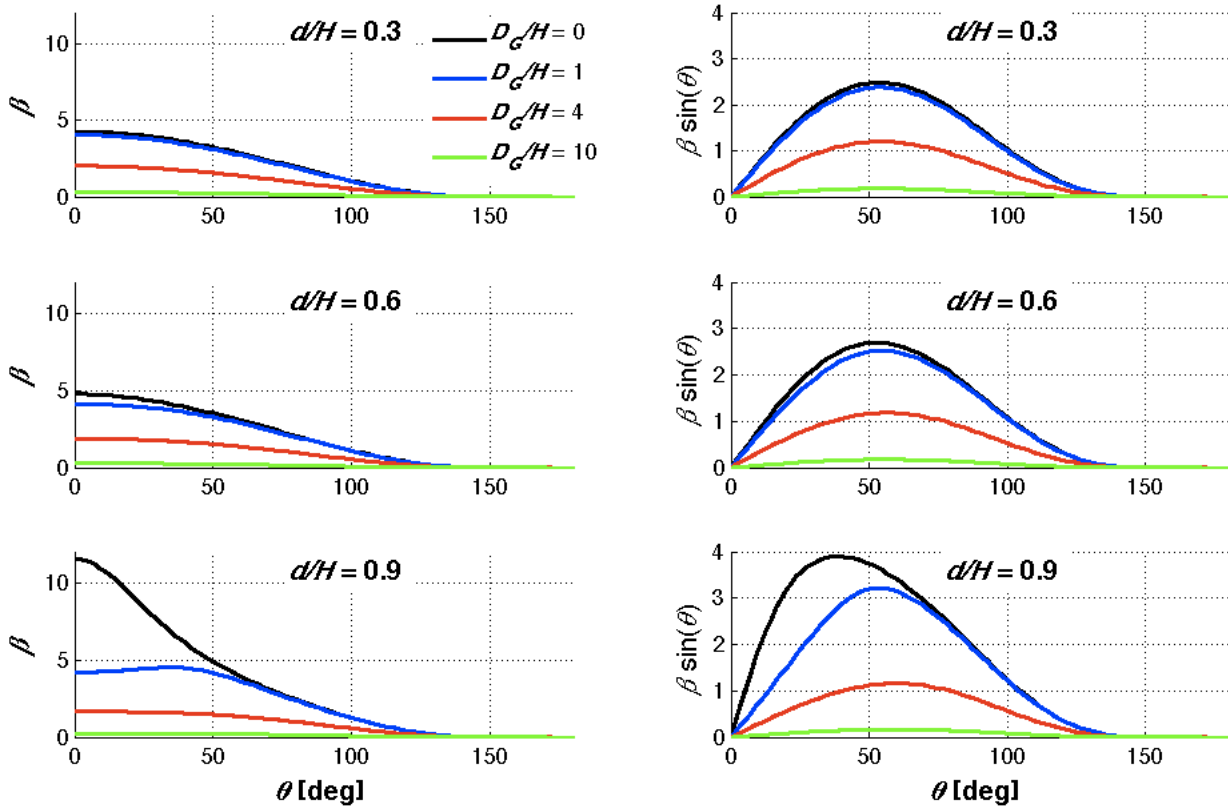


Figure 5. Electric field behavior at isolated particle surface for gated-electrode configuration. Field enhancement factor β is proportional to the surface charge density. The area under the $\beta \sin \theta$ curve is proportional to the particle charge for a given particle size.

In general, the peak electric field occurs at the particle tip ($\theta = 0$). Exceptions occur for $d/H > 0.6$ and $D_G/H < 3$, where the edges of the gate orifice approach the particle surface and effects due to the gate thickness are apparent. At a given d/H , both the surface electric field and the integrated field enhancement factor decrease as the gate orifice diameter increases. For a given gate aspect ratio (i.e., constant D_G/H), larger particles (i.e., larger d/H) result in higher peak surface electric fields and larger integrated field enhancement factors. Note that for cases where $D_G/H = 0$, thus recovering the parallel-electrode configuration, the calculated particle charges agree well with Félici's model.

For example, at $d/H = 0.1$ and $d/H = 0.3$, the calculated charges deviate from Félici's model by only 0.03% and 1%, respectively, which serves to validate the simulations.

The presence of the gate orifice results in a particle charge $q_2 < q_1$, the particle charge with no gate orifice. This decrease in contact charging is represented by the charging factor shown in Figure 6:

$$\alpha_{21}(d, D_G, H) \equiv \frac{q_2}{q_1}. \quad (7)$$

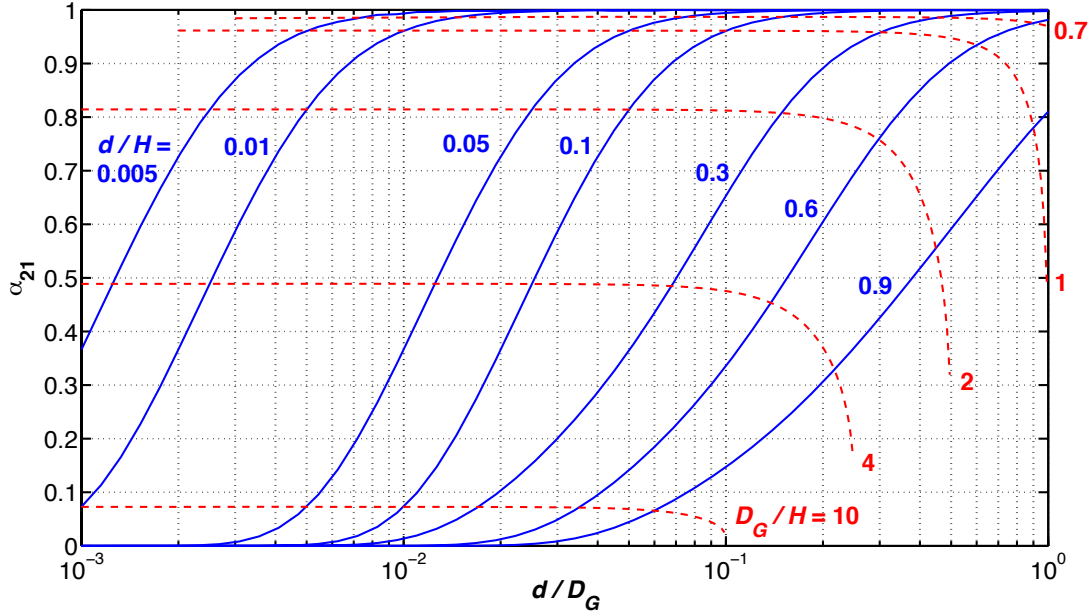


Figure 6. Charging factor for gated-electrode configuration. Particle extraction is possible for $d/D_G < 1$.

As d/D_G increases, the charging factor α_{21} approaches unity, thus recovering the parallel-electrode configuration. At a given particle size and H , α_{21} decreases with larger gate orifice diameters; at a given particle size and D_G , α_{21} increases with larger inter-electrode gaps. Thus, for a given particle size, a smaller gate aspect ratio D_G/H provides a greater charging factor. For example, $\alpha_{21} > 0.96$ for $D_G/H \leq 1$ and $d/H < 0.3$. Note that for a fixed gate configuration (i.e., both D_G and H are fixed), two distinct regimes exist for the charging factor's behavior. The charging factor remains essentially constant for small particles and decreases rapidly for $d/H > 0.6$.

The saturation charge for an isolated particle in the gated electrode configuration is thus

$$q_2 = \alpha_{21} \alpha_{10} q_0 = \alpha_{20}(d, D_G, H) q_0, \quad (8)$$

where α_{20} is the net charging factor in a gated-electrode configuration. In Figure 7 as the gate aspect ratio D_G/H increases, α_{20} decreases; equivalently, for a given particle size and H , α_{20} decreases for larger gate orifice diameters. In the case $D_G/H = 0$, recovery of the parallel-electrode configuration means that $\alpha_{20} = \alpha_{10}$. Note that the net charging factor is insensitive to d/H for $d/H < 0.5$. While having both large d/H and small D_G/H (or equivalently, large d/D_G) provide net charging factors greater than unity, caution is needed due to the large field enhancement in these cases (Figure 5). A more conservative approach to optimizing the net charging factor would be to have $d/H \leq 0.5$ and $D_G/H \leq 1$ to reduce the likelihood of having electric fields that exceed the field emission/evaporation limit.

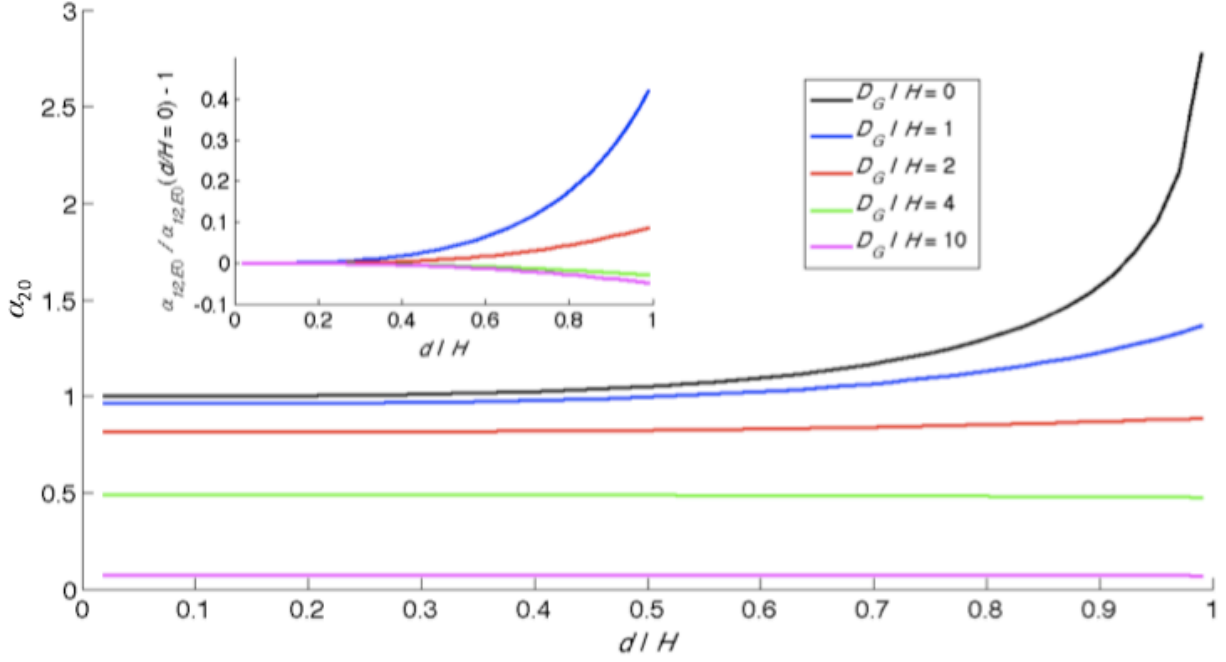


Figure 7. Net charging factor for gated-electrode configuration. Inset figure shows the net charging factor's deviation from its value at $d/H = 0$.

3. Proximal Particle Effects

The presence of nearby particles results in a particle charge $q_{2p} < q_2$, the particle charge when in isolation. This decrease in particle charge is represented by the charging factor

$$\alpha_{2p}(d, D_G, H, R) \equiv \frac{q_{2p}}{q_2}. \quad (9)$$

The net charging factor with proximal particles taken into account thus becomes

$$\alpha_{2p0}(d, D_G, H, R) = \frac{q_{2p}}{q_0} = \alpha_{2p} \alpha_{21} \alpha_{10}. \quad (10)$$

Preliminary simulation results suggest that $\alpha_{2p0} > 0.9$ for $R/d > 5$. This suggests that to maximize charging, individual NanoFET extractors (i.e., sieve holes) should have a pitch that is at least five times larger than the hole diameter.

B. Particle Mass in NanoFET

As shown in Equation 1 for contact charging, particles of the same size acquire the same charge for a given electric field. A particle with lower mass density, therefore, would have less mass than its higher mass density counterpart, thus resulting in a higher specific charge. Lower mass density may also be achieved by using hollow rather than solid particles. The specific charge enhancement factor $\alpha_{q/m}$ for a hollow particle of shell wall thickness t_w compared to a solid particle of the same diameter d is

$$\alpha_{q/m} \equiv \frac{(q/m)_h}{(q/m)_s} = \frac{m_s}{m_h} = \frac{\rho_s}{\rho_h} \left[1 - \left(1 - 2 \frac{t_w}{d} \right)^3 \right]^{-1}, \quad (11)$$

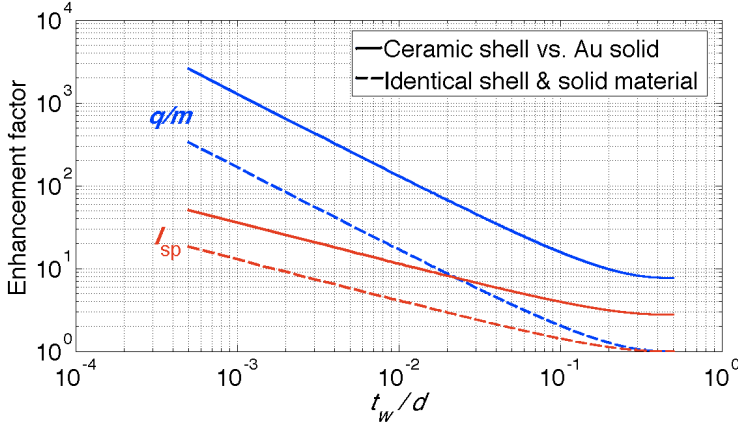


Figure 8. Enhancement of specific charge and specific impulse for hollow compared to solid particles. Ceramic shells ($\rho_h = 2.5 \text{ g/cm}^3$) are assumed to be either semiconducting or to have a thin metal coating for contact charging.

I_{sp} gains, the mechanical robustness of the thin-shell particles also becomes a concern. Note that solid or hollow ceramic (metallized¹¹ or semiconductor¹²) particles, with sufficient electrical conductivity due to inherent semiconductivity or metallization, already exist with t_w/d approaching 5%.

C. Performance Predictions

Figure 9 shows predictions for NanoFET's achievable I_{sp} and thrust-to-power for various propellant types, including metal shell particles¹³, when particle charging is optimized (i.e., near-unity net charging factor).

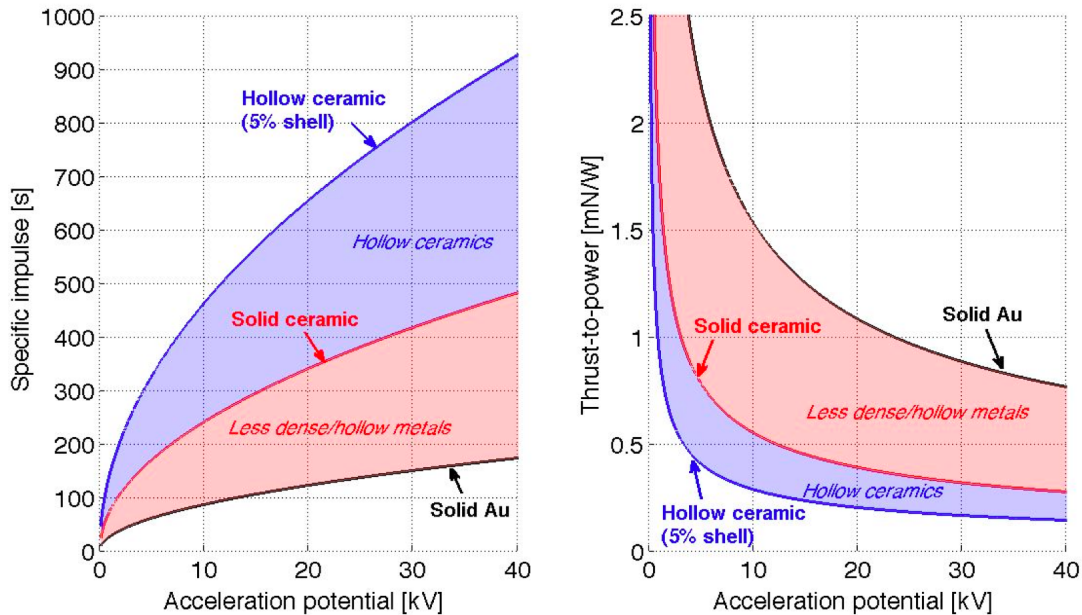


Figure 9. Predicted NanoFET performance for 50-nm particles charging in $400\text{-V}/\mu\text{m}$ electric fields. 2.5 g/cm^3 is used as the mass density of ceramic materials, which are assumed to be either semiconducting or to have a thin metal coating for contact charging. The hollow ceramic particles are shown with shell wall thicknesses greater than 5% of the particle diameters.

50-nm particles are assumed to undergo classical contact charging in $400\text{-V}/\mu\text{m}$ background electric fields in gate geometries. While higher charging fields may be possible to achieve higher specific charges, given by

$$\alpha_{I_{sp}} \equiv \frac{(I_{sp})_h}{(I_{sp})_s} = \sqrt{\alpha_{q/m}} \quad (12)$$

Both enhancement factors are shown in Figure 8. In the case of dissimilar materials between the shell and solid particles, gold solids and ceramic shells are chosen to illustrate the enhancement. While having small t_w/d yields greater specific charge and

$$\frac{q}{m} = \pi^2 \frac{\epsilon E_0}{\rho_s d} \alpha_{2p0} \alpha_{q/m}, \quad (13)$$

issues of approaching the electron field emission limit or the electric breakdown strength of the gate spacer material must be carefully evaluated. Smaller particles may also be used to achieve higher specific charges, albeit with a need to overcome more significant particle adhesive and cohesive forces. For acceleration potentials on the order of tens of kilovolts, NanoFET is predicted to achieve specific impulses of hundreds of seconds for 50-nm particles. These moderate I_{sp} values result in high thrust-to-power ($T/P = 2\eta/g_0 I_{sp}$) performance predictions for NanoFET, with possible T/P in excess of 1 mN/W.

III. Overcoming Adhesive and Cohesive Forces

For the particles to be extracted after charging, the adhesive and cohesive forces F_r holding the particles to the charging electrode and to each other, respectively, must be overcome. Consider the particle being charged in Figure 3. The net restraining (adhesive) force scales linearly with particle size as

$$F_r = \frac{1}{12} \frac{H_A}{a_0^2} d, \quad (14)$$

with Hamaker constant H_A and a_0 typically set at 0.4 nm.¹⁴ This restraining force may be overcome by applying a sufficiently high electric field. The resulting electrostatic force F_E for an optimally charged particle (i.e., near-unity net charging factor) is

$$F_E = \frac{\pi^3}{6} \gamma \epsilon E_0^2 d^2, \quad (15)$$

with $\gamma = 0.832$ to account for the image charge effect.⁴ The electric field E_L required for particle liftoff from the electrode thus satisfies

$$E_L^2 = \frac{1}{2\pi^3} \frac{H_A}{\gamma \epsilon a_0^2} d^{-1}. \quad (16)$$

For a given charging electric field, treating and functionalizing particle surfaces to modify their effective Hamaker constants and reduce adhesive and cohesive forces is one approach to permit particle liftoff. Using lower density and hollow particles also helps because larger particles could be used to meet a given I_{sp} target; adhesion and cohesion issues are less significant for larger particles, thus improving the propellant's dry storage capability and reducing the risk of feed system jamming in NanoFET.

NanoFET's piezoelectric feed system, using low-power piezoelectric thin films¹⁵, can be used to control particle extraction in addition to facilitating particle passage through the charging sieve. With the piezoelectric, an inertial force that varies quadratically with the applied sinusoidal oscillation frequency f may be applied to the particle. As a result, the required liftoff electric field may be reduced by

$$\Delta E_L^2 = 4 \frac{\rho_s x_{ppk} f^2}{\alpha_{q/m} \gamma \epsilon} d, \quad (17)$$

with piezoelectric peak-to-peak oscillation amplitude x_{ppk} . Therefore, the particle may be charged at the reduced liftoff electric field, but particle extraction and acceleration would not occur until the piezoelectric is activated, with each piezoelectric actuation lifting off a single particle layer. The piezoelectric thus serves to regulate the mass flow rate of the NanoFET system. In general, the piezoelectric oscillation period ($> 1 \mu s$) is much greater than the time scales associated with particle charging or transit through the gates and thus serves as the characteristic time scale for particle extraction. Note that other actuation waveforms (e.g., square wave pulses) may also be used.

In Figure 3, the thrust T_0 during continuous NanoFET operations from a single particle extraction site becomes, for optimally charged particles (i.e., near-unity net charging factor),

$$T_0 = \frac{\pi^2}{6} \left(\frac{2\epsilon E_0 V \rho_s}{\alpha_{q/m}} d^5 \right)^{\frac{1}{2}} f. \quad (18)$$

Note that for a single extractor, the impulse T_0/f per piezoelectric actuation represents the minimum impulse bit, which is provided when NanoFET is operated in pulsed mode.

IV. Conclusion

To answer the two key challenges posed in the introduction of this paper:

- 1) To meet propulsive performance targets with reasonable acceleration potentials, high specific charge is desirable. Charging may be optimized to have a near-unity net charging factor while remaining below the field emission/evaporation limit for $D_G/H \leq 1$, $d/H \leq 0.5$, and $R/d \geq 5$. For the same particle size, lower mass density or hollow particles provide a greater specific charge.
- 2) In addition to applying high charging fields and tailoring the surface properties of particles and the charging sieve, NanoFET's piezoelectric feed system provides a mechanism to reliably impart inertial forces to facilitate particle liftoff.

With these design configurations implemented, NanoFET is predicted to achieve hundreds of seconds of I_{sp} with tens of kilovolts of acceleration potentials. Such moderate specific impulses provide NanoFET with high thrust-to-power capabilities. NanoFET's piezoelectric feed system also has the potential to provide precise thrust control in continuous and pulsed operations. These promising capabilities would permit NanoFET great flexibility in adapting to changing mission needs using a single engine — missions that would otherwise need multiple different propulsion systems with attendant increased propulsion system mass and more complicated spacecraft design and integration.

Acknowledgements

The work presented was funded in part by an Air Force Office of Scientific Research Phase 2 STTR (FA9550-09-C-0079, managed by Dr. Mitat Birkan) and a National Science Foundation Graduate Research Fellowship (Liu). Thanks to Harvey Elliott, Shane Moore, Greg Salvesen, and Yuly Wung at the University of Michigan for their initial studies of particle contact charging using COMSOL.

References

- ¹ Massey, D., Musinski, L., Liu, T., Gallimore, A., and Gilchrist, B., "The Nanoparticle Field Extraction Thruster: NanoFET," JANNAF 3rd Spacecraft Propulsion Subcommittee Meeting, Orlando, FL, 8-12 December 2008.
- ² Liu, T., Musinski, L., Patel, P., Gallimore, A., Gilchrist, B., and Keidar, M., "Nanoparticle Electric Propulsion for Space Exploration," in *Space Technology and Applications International Forum – STAIF 2007*, edited by M. S. El-Genk, American Institute of Physics, Albuquerque, NM, 2007, pp. 787-94.
- ³ Musinski, L., Liu, T., Gilchrist, B., Gallimore, A., and Keidar, M., "Scalable Flat-Panel Nano-Particle MEMS/NEMS Thruster," IEPC-2005-176, 29th International Electric Propulsion Conference, Princeton, NJ, 31 October – 4 November 2005.
- ⁴ Félici, N.-J., "Forces et Charges de Petits Objets en Contact avec une Électrode Affectée d'un Champ Électrique," *Revue Générale de l'Électricité*, **75** (1966), pp. 1145-60.
- ⁵ Trottenberg, T., Kersten, H., and Neumann, H., "Feasibility of Electrostatic Microparticle Propulsion," *New Journal of Physics*, **10** (2008).
- ⁶ Tobazéon, R., "Electrohydrodynamic Behaviour of Single Spherical or Cylindrical Conducting Particles in an Insulating Liquid Subjected to a Uniform DC Field," *J. Phys. D: Appl. Phys.*, **29** (1996), pp. 2595-608.
- ⁷ Musinski, L., Liu, T., Gilchrist, B., and Gallimore, A., "Electrostatic Charging of Micro- and Nano-Particles for Use with Highly Energetic Applications," *Journal of Electrostatics*, 4 November 2008, pp. 1-8.
- ⁸ Musinski, L., "Investigation of a Micro- and Nano-Particle In-Space Electrostatic Propulsion Concept," Ph.D. dissertation, University of Michigan, 2009.
- ⁹ Nader, B.F., Castle, G.S.P., and Adamiak, K., "Effect of Surface Conduction on the Dynamics of Induction Charging of Particles," *J. Electrostatics*, **67** (2009), pp. 394-9.
- ¹⁰ Yu, D., Castle, G.S.P., and Adamiak, K., "The Effect of Shape and Roughness on the Maximum Induction Charge for Small Particles," *J. Phys.: Conf. Ser.*, **142** (2008).
- ¹¹ Hirsch, L.R., Gobin, A.M., Amanda, R.L., Tam, F., Drezek, R.A., Halas, N.J., and West, J.L., "Metal Nanoshells," *Annals of Biomedical Engineering*, **34** No. 1, (2006), pp. 15–22.
- ¹² Koktysh, D.S., Liang, X., Yun, B.-G., Pastoriza-Santos, I., Matts, R.L., Giersig, M., Serra-Rodríguez, C., Liz-Marzán, L.M., and Kotov, N.A., "Biomaterials by Design: Layer-by-Layer Assembled Ion-Selective and Biocompatible Films of TiO₂ Nanoshells for Neurochemical Monitoring," *Advanced Functional Materials*, **12** No. 4 (2002), 255-65.
- ¹³ Graf, C. and van Blaaderen, A., "Metallo-dielectric Colloidal Core-Shell Particles for Photonic Applications," *Langmuir*, **18** (2002), pp. 524-34.
- ¹⁴ Bowling, R., "Analysis of Particle Adhesion on Semiconductor Surfaces," *J. Electrochem. Soc.*, **132** (1985), pp. 2208-14.
- ¹⁵ Aktakka, E.E., Kim, H., and Najafi, K., "Wafer-Level Fabrication of High Performance MEMS Using Bonded and Thinned Bulk Piezoelectric Substrates," 15th International Conference on Solid-State Sensors, Actuators, and Microsystems (Transducers 2009), Denver, CO, June 2009, pp. 849-52.